LAWRENCE
LIVERMORE
NATIONAL
LABORATORY

LLNL-PROC-498671

Microarcsecond relative astrometry from the ground with a diffractive pupil

S. Mark Ammons, E. Bendek, O. Guyon

September 9, 2011

SPIE Optics & Photonics
San Diego, CA, United States
August 21, 2011 through August 25, 2011

Disclaimer

Microarcsecond relative astrometry from the ground with a diffractive pupil

S. Mark Ammons*[a], Eduardo A. Bendek[b], Olivier Guyon[b,c]

[a]Lawrence Fellow, Lawrence Livermore National Laboratory, Physics Division, L-210, 7000 East Ave., Livermore, CA USA 94550
[b]Steward Observatory, University of Arizona, 933 Cherry Ave, Tucson, AZ USA 95060
[c]Subaru Telescope, 640 N. Aohoku Place, Hilo, HI, US

ABSTRACT

The practical use of astrometry to detect exoplanets via the reflex motion of the parent star depends critically on the elimination of systematic floors in imaging systems. In the diffractive pupil technique proposed for space-based detection of exo-earths, extended diffraction spikes generated by a dotted primary mirror are referenced against a wide-field grid of background stars to calibrate changing optical distortion and achieve microarcsecond astrometric precision on bright targets (Guyon et al. 2010). We describe applications of this concept to ground-based uncrowded astrometry using a diffractive, monopupil telescope and a wide-field camera to image as many as ~4000 background reference stars. Final relative astrometric precision is limited by differential tip/tilt jitter caused by high altitude layers of turbulence. A diffractive 3-meter telescope is capable of reaching ~35 μas relative astrometric error per coordinate perpendicular to the zenith vector in three hours on a bright target star ($I < 10$) in fields of moderate stellar density (~40 stars arcmin^{-2} with $I < 23$). Smaller diffractive apertures ($D < 1$ m) can achieve 100-200 μas performance with the same stellar density and exposure time and a large telescope (6.5-10 m) could achieve as low as 10 μas, nearly an order of magnitude better than current space-based facilities. The diffractive pupil enables the use of larger fields of view through calibration of changing optical distortion as well as brighter target stars ($V < 6$) by preventing star saturation. Permitting the sky to naturally roll to average signals over many thousands of pixels can mitigate the effects of detector imperfections.

Keywords: astrometry, diffractive pupil, microarcsecond, SIM, PECO, differential atmospheric refraction, extrasolar planet, exoearth, differential tip/tilt jitter

1. INTRODUCTION

1.1 The Need for Microarcsecond Relative Astrometry from the Ground

The GAIA mission will provide relative astrometry at the ~25 microarcsecond level for a billion stars as faint as V ~ 15 over its mission lifetime.[1,2] Such precision will be important for estimating parallactic distances for stars near the Galactic bulge, discovering new brown dwarf and planetary companions to nearby stars, and estimating orbital parameters for hundreds of thousands of minor planets and asteroids in the Solar System. Although GAIA's astrometric precision over its mission lifetime is a substantial gain over previous surveys like Hipparcos,[3] the survey is not targeted and will not optimize observational cadence for individual stars. Targeted surveys can tune observing strategies to the scientific objectives for a particular star. For example, a targeted astrometric survey with equivalent astrometric precision to GAIA would be able to follow-up radial velocity (RV) detections of faint companions with known orbits more efficiently or even detect rocky planets around nearby brown dwarfs.

The astrometric precision necessary for detecting planets around a reasonable number of nearby stars is ~30-100 μas. The astrometric signal produced by a Jupiter-mass planet orbiting a K star with a semimajor axis of 1 astronomical unit

*ammons1@llnl.gov; phone 1 925 422-2102; www.u.arizona.edu/~ammons81/

(AU) 10 parsecs away from the sun is ~150 μas. A Saturn-mass planet in a similar configuration would produce a ~45 μas signal. Relative astrometric precision at the ~100-300 μas level with a single aperture has been claimed with VLT/FORS2,[4] VLT/NACO with adaptive optics,[5] Keck NIRC2 with adaptive optics,[6] the Palomar 5-meter telescope in the seeing limit[7] and assisted with adaptive optics,[8] and many others. However, the theoretical astrometric precision attainable in these observations (10-30 μas) is typically an order of magnitude smaller than that verified by observation,[8] suggesting that some systematic noise floor is being reached. In many cases, the noise floor is associated with stellar crowding which complicates extraction and modeling of Point Spread Functions (PSFs).[9,10] In uncrowded fields, the systematic noise floor may be dominated by instrumental jitter.

Here we consider two major sources of instrumental jitter: Changes in the telescope distortion field with time and detector imperfections. Dynamic distortion errors may be induced by temperature fluctuations, movement of optics, or changes in the properties of the optics themselves. Much attention has been paid to reducing the effects of changes in the distortion field, including frequent on-sky calibration using star clusters[11] and extensive internal calibration. Detector imperfections may include flat-fielding errors, hot pixels, insufficient linearity, and most importantly, changes in these parameters with time.

1.2 The Diffractive Pupil and Slow Telescope Roll Techniques

The diffractive pupil and slow telescope roll techniques have been presented as solutions to several dominant sources of systematic instrumental jitter in space-based telescopes intending to detect planets astrometrically.[12,13] The *diffractive pupil* places a grid of dots on the primary mirror of the telescope to induce polychromatic diffraction spikes in the PSF. The diffraction spikes from a bright, central target star follow similar optical paths to nearby reference stars in the field, tracing the distortion map and thus calibrating changes in the distortion in real time. The relative distances between reference stars and the target star are measured with respect to the nearest diffraction spike and not the image of the target star itself, which is usually saturated.

The length and orientation of the diffraction spikes can be tuned to densely sample the distortion grid in the focal plane. The pattern of dots must be imprinted on the first optic in the system to fully trace all instrumental distortion induced by motion of the primary. Although the reference stars produce diffraction spikes as well as the target star, the reference stars are typically many orders of magnitude fainter than the target star (V ~ 6-12) so that their diffraction spikes do not add significantly to the background of the image.

The *slow telescope roll* involves a telescope rotation during a single epoch to trace the paths of the reference stars and diffraction spikes over many pixels, thus averaging out the effects of detector imperfections. The principles of operation of the diffractive pupil and telescope roll are described in detail in other publications.[12,13,14]

In this paper, we investigate the relative astrometric precision obtainable from the ground with monopupil telescopes assuming that both the diffractive pupil and telescope roll techniques are applied. We consider the dominant error budget terms widely discussed in the literature but do not intend the simulations to be exhaustive. In Section 2, we construct a simulation of the astrometric performance of the telescope, describe the simulated observational parameters, and list the error budget terms included. Section 3 presents results and Section 4 concludes. Vega magnitudes are assumed unless noted otherwise.

2. SIMULATIONS

We now focus on the range of science cases targeting a single bright star ($V < 12$) using a reference grid of many background stars ($N > 25$) over a wide field ($d > 1'$). This excludes science cases in crowded fields such as globular clusters or the Galactic Center, where errors in extracting star positions are complicated by significant overlap of adjacent point spread functions (PSF) and adaptive optics observations are critical for resolving stars.[6]

Below, we present estimates of the relative, single-epoch astrometric precision per coordinate obtained on a bright star of magnitude m in band B with a ground-based mono-pupil telescope and wide-field imaging detector. The precision is estimated as a function of telescope diameter D, field diameter d, integration time t, zenith angle ξ, and Galactic latitude b.

2.1 Simulation Assumptions

We model the distribution and brightnesses of the reference star grid with the Bahcall & Soneira (1980) star count model as provided in the fortran "BSGmodel" code.[15] The star counts are interpolated over the V-band magnitude range $4 < V < 24$ and the Galactic latitude range $20° < b < 90°$. Star counts are obtained at a Galactic latitude of 5° by interpolating J-band counts from the UKIDSS Galactic Plane Survey (GPS) survey.[16] To obtain counts in the I-band, mean colors of $V - I = 1.0$ for $b > 20°$ and $I - J = 1.1$ for $b = 5°$ are assumed, which are estimated using FGK-type dwarf colors with Galactic extinction from Schlegel et al. (1998) dust maps.[17] For a simulated circular field of view of diameter d at a Galactic latitude b, reference stars are inserted in random locations in the field according to the Bahcall & Soneira probability distribution. Poisson statistics are assumed.

The imaging telescope is assumed to be circular with 30% overall system throughput (including atmosphere, optics, and detector efficiencies) and a 10% obscuration fraction from a secondary mirror. Conventional CCD detector technologies are assumed. The bandpass is centered on the infrared band (Johnson I-band) to minimize chromatic differential atmospheric refraction (CDAR) error, which decreases with wavelength. The seeing is assumed to be 0.8″ and the sky background assumed to be $I = 20.0$ Vega magnitudes per square arcsecond. The detector is assumed to have 0.12″ pixels to sample at better than Nyquist for nearly all seeing conditions.

The exposure time of individual frames within a total exposure is set to 10 seconds, approximately equal to the readout time of standard CCDs. Shorter exposures of individual frames would hurt the overall time-efficiency of the visit. Longer exposures would blur the stars near the edge of the largest fields studied (d ~ 8′) by more than 0.2″ as the sky rotates, a significant fraction of the seeing. Assuming a full-well depth of 50,000 electrons, this exposure also sets the star magnitude at which the detector saturates for a given telescope size. With the detection efficiencies and reference star grid chosen, this saturation limit cuts stars from the reference grid for telescope diameters larger than ~2 meters ($I_{sat} = 11.5$). Larger telescopes (D ~ 10 m) lose significant numbers of bright stars from the reference grid to saturation.

We assume that the primary mirror of the telescope has been imprinted with a hexagonally-distributed dotted matrix. Ten percent of a star's light is assumed to be in its diffraction spikes. The size and separation of the dots on the primary mirror is set to produce 50 visible spikes within the field of view from the primary star. The slow telescope roll is implemented with an *alt-az* telescope design, in which the sky is permitted to naturally rotate across the field of view while the central target star is tracked. During typical ~3 hour observations, the sky rotates by 45 degrees. A full, closed rotation is not required to gain the pixel-averaging benefits of the technique.[12]

To substantially reduce error associated with differential atmospheric refraction (DAR), we ignore the measured astrometric coordinate perpendicular to the zenith vector for any given reference star. Typical observations will constrain both x- and y- position coordinates of the target star as a field transits the meridian and the zenith vector rotates through 90 degrees. Exceptions include fields at low declination ($\delta < -20°$) for northern telescopes, whose observation windows are too short to rotate the zenith vector through 90 degrees. In addition, for fields that transit the zenith using equatorial telescopes, the East-West coordinate of motion is only measurable for a short time as the field transits.

2.2 Covariance-Based Weighting Method

In constructing a reference grid of background stars, we assemble a vector of weights $\boldsymbol{W}$ to penalize stars with noisy centroids and promote stars with more secure positions. To derive these weights, we turn to the covariance matrix-based framework of Cameron, Britton, & Kulkarni (2009)[8] to minimize the expected variance of the target star with respect to the covariance for Differential Tip/Tilt Jitter (DTTJ, described in Section 2.3.1), measurement error, residual chromatic and achromatic differential atmospheric refraction, and residual instrumental jitter due to changes in optical distortion. We describe each of these terms below.

2.3 Individual Astrometric Error Terms

2.3.1. *Differential Tip/Tilt Jitter (DTTJ).* DTTJ refers to error in measuring the relative positions of two stars caused by de-correlation of atmospheric tilt on the two columns of atmosphere pointing to the stars. DTTJ is closely tied to the strength of high-altitude layers of turbulence. The full equation for DTTJ error as a function of star separation, atmospheric properties, and telescope aperture size is given by Sasiela (2007)[18]:

$$\begin{bmatrix}\sigma_{\parallel}^2\\ \sigma_{\perp}^2\end{bmatrix} = \frac{6.08}{D^{1/3}}\int_0^{H_c} dz\, C_N^2(z)\left\{\begin{bmatrix}1.316\left(\frac{\theta z}{D}\right)^2\ {}_5F_4\left[\frac{7}{6},-\frac{17}{6},-\frac{5}{6},\frac{5}{2},1;-\frac{1}{3},3,\frac{3}{2},2;\left(\frac{\theta z}{D}\right)^2\right]\\ 0.4392\left(\frac{\theta z}{D}\right)^2\ {}_4F_3\left[\frac{7}{6},-\frac{17}{6},-\frac{5}{6},1;-\frac{1}{3},3,2;\left(\frac{\theta z}{D}\right)^2\right]\end{bmatrix}\right.$$
$$\left.+\begin{bmatrix}2.195\left(\frac{\theta z}{D}\right)^{14/3}\ {}_4F_3\left[\frac{5}{2},-\frac{3}{2},\frac{1}{2},\frac{23}{6};\frac{17}{6},\frac{13}{3},\frac{10}{3};\left(\frac{\theta z}{D}\right)^2\right]\\ 0.388\left(\frac{\theta z}{D}\right)^{14/3}\ {}_3F_2\left[\frac{5}{2},-\frac{3}{2},\frac{1}{2};\frac{13}{3},\frac{10}{3};\left(\frac{\theta z}{D}\right)^2\right]\end{bmatrix}\right\}$$
$$+\frac{6.08}{D^{1/3}}\left\{\sec\xi\int_{H_c}^{\infty} dz\, C_N^2(z) - \int_{H_c}^{\infty} dz\, C_N^2(z)\begin{bmatrix}0.531\left(\frac{D}{\theta z}\right)^{1/3}\ {}_4F_3\left[-\frac{5}{6},\frac{5}{2},\frac{1}{6},\frac{2}{3};5,3,-\frac{1}{3};\left(\frac{D}{\theta z}\right)^2\right]\\ 0.798\left(\frac{D}{\theta z}\right)^{1/3}\ {}_3F_2\left[-\frac{5}{6},\frac{5}{2},\frac{1}{6};5,3;\left(\frac{D}{\theta z}\right)^2\right]\end{bmatrix}\right\}$$

where $H_c = (D/\theta)\cos\xi$ and ${}_pF_q$ are the generalized hypergeometric functions defined by

$${}_pF_q[(a);(b);z] - 1 = z\frac{\prod_{n=1}^{p} a_n}{\prod_{n=1}^{q} b_n}\,{}_{p+1}F_{q+1}[(a+1),1;(b+1),2;z]$$

The DTTJ error is plotted against the star separation for different aperture sizes in Figure 1. A Mauna Kea-type C_N^2 is assumed.[19] In crowded field scenarios, with typical star separations of less than 20″, the DTTJ error worsens sharply with increasing separation. For wide-field cases (d >1′), the DTTJ error is nearly flat with separation. The difference in DTTJ error between an 8-meter aperture and a 1-meter aperture decreases at large separations. The DTTJ error is assumed to average down with the integration time as the square root of τ/t, where τ is the wind crossing time of the telescope.[8] The wind speed is set to 25 m/s to match similar observational studies on Palomar.[8]

2.3.2. *Star SNR*. The theoretical centroiding limit of a well-sampled, Gaussian star image with full-width at half-maximum (FWHM) of s is[20]

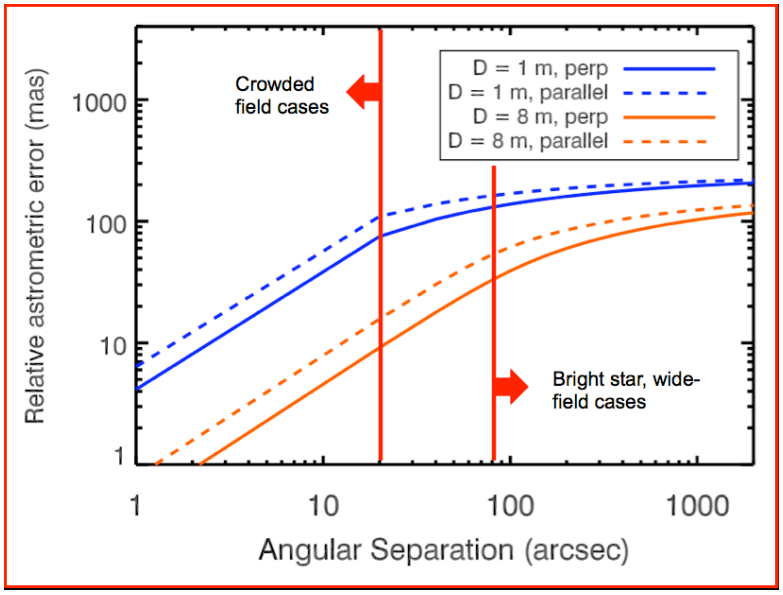

Fig. 1. Relative astrometric error due to Differential Tip/Tilt Jitter in milliarcseconds as a function of angular separation in arcseconds. Blue lines are for a 1-meter collecting aperture and red lines are for an 8-meter aperture. Dashed and solid lines denote the components of astrometric error parallel and perpendicular to the vector connecting the stars, respectively. These lines are for an integration time equal to the wind crossing time of the telescope.

$$\sigma = \frac{s}{\pi\, SNR}$$

where SNR is the signal-to-noise ratio of the star detection. We assume 4 e^-/pix read noise, 0.12″ pixels, negligible dark current, and a sky background of $I = 20$ magnitudes arcsec^{-2}.

2.3.3. *Differential Atmospheric Refraction (DAR).* The atmosphere acts as a refracting prism, changing the apparent separation ΔR between two stars with a dependence on the zenith angle ξ: [21]

$$\Delta R = (1+\tan^2\xi)\left\{(A+3B\tan^2\xi)\Delta\xi - \left[A\tan\xi + 3B(\tan\xi + 2\tan^3\xi)\right]\Delta\xi^2\right\}$$

where $\Delta\xi$ is the separation of the stars in radians and A and B are wavelength-dependent constants in arcseconds given in Gubler & Tytler (1998).[21] A maximum star separation of 4 arcminutes in the I-band with $\xi = 30°$ gives a first order term of ~73.5 mas and a second order term of ~48 μas. For large numbers of reference stars (N > 25), both terms can be fitted and removed with first and second-order transformations. In a single integration, third-order terms and fitting errors parallel to the zenith vector are reduced to the sub-microarcsecond level for star separations of a few arcminutes. Perpendicular to the zenith vector, the error is further attenuated by a factor equal to the angular error in knowledge of the zenith direction. For an estimation error of ~1 arcminute in this parameter, the error perpendicular to the zenith direction is much less than one microarcsecond.

2.3.4. Chromatic Differential Atmospheric Refraction (CDAR). The differential atmospheric refraction effect also has a chromatic term that depends on the colors of two stars being compared. Gubler and Tytler (1998) show that this error term can be reduced to ~100 μas for measurement of the separation of two stars (K-band, $\xi = 30°$) with incorporation of an atmospheric model. This model requires knowledge of the zenith position to ~36″, the ground temperature to ~0.6 K, the ground pressure to 1.6 mB, the relative humidity to ±10%, and the temperature of both stars to ~100 K for cool stars and ~1000 K for hot stars. This method is currently employed to reduce astrometric error due to CDAR in observations of the Galactic center.[22,23] Even after applying a correction derived from atmospheric models, CDAR error is considerably larger at optical wavelengths,[24] approaching 1-2 mas in I-band for two stars ($\xi = 30°$).

However, as for achromatic DAR, the error perpendicular to the zenith angle is a small fraction of the error parallel to the zenith angle. The CDAR error perpendicular to the zenith angle is less than one microarcsecond for an error of ~1 arcminute in the estimation of the zenith position. To reduce the effects of chromatic differential atmospheric refraction in this study, we report the component of astrometric error perpendicular to the zenith vector for all further results.

2.3.5. PSF Modeling and Pixel Sampling Errors. Two important sources of astrometric error are associated with pixel sampling and the exact methodology used for centroiding. In particular, undersampling the Point Spread Function (PSF) can induce "pixel-phase" error, in which the recovered centroid is a function of the position of the center of mass of the PSF within a pixel.[25] Pixel-phase errors can be reduced to near-zero by critically sampling the PSF.[26] With 0.12″ pixels, our model observations are robust to pixel-phase error for nearly all atmospheric conditions.

Crowding errors appear when modeling and extracting PSFs from closely-spaced stars whose PSFs overlap. This error is not important for even the densest fields we investigate (~40 stars arcmin^{-2}). We do not consider the effects of faint background galaxies in modeling of the PSF, but note that only relative, epoch-to-epoch changes in the geometric overlap of reference stars and background galaxies are important. Such changes can be induced by the proper motion of the reference stars. For observations near the Galactic disc ($-10° < b < 10°$), the majority of reference stars will be nearby FGK dwarfs at ~1 kpc and brighter red giants at ~10 kpc. Few of these reference stars will have a parallax or proper motion higher than ~5 mas/year, which would induce significant PSF modeling errors if the star overlapped with a bright galaxy ($I \sim 20$). We note also that noisy stars can be flagged and removed from the reference grid.

It is assumed that field-dependent models of the PSF can be obtained for cross-correlation or deconvolution from the brightest stars in the stacked images of the field or using a StarFinder-like technique.[27] The diffraction spikes produced by the target star are convolved with the target star's PSF, which can be estimated from the nearest bright reference stars. Astrometric errors are induced when the *spatial distribution* of the PSF changes with time. Any changes in the high-order wavefront that cause spatially-varying movements in the center-of-mass of the PSF are captured in the statistics of the Differential Tip/Tilt Jitter error term, so we do not include a separate error term for PSF modeling.

The sky is allowed to rotate with respect to the detector to average over flat-fielding errors in the detector. It is assumed that these errors average down with the square root of the number of pixels. With realistic assumptions for the amplitude of flat-fielding errors and nonlinearities, simulations indicate that errors due to detector imperfections can average down to the sub-microarcsecond level.[12,13]

2.3.5. Static and Dynamic Distortion Errors. It is assumed that the static distortion of the detector is known at the ~10 mas level through on-sky calibration techniques such as cluster observations (e.g., Anderson & King 2003). For comparison, the static distortion of the Hubble Space Telescope WFPC2 chip and the Keck NIRC2 narrow-field chip have been calibrated to better than 1 mas.[11,23]

The diffractive pupil technique calibrates the dynamic distortion changes of the telescope during observations.[12] The technique is limited principally by the sampling of the distortion field by the diffraction spikes of the target star. The factor by which the distortion errors are reduced is a function of the average spike separation (~5-20" for the models investigated), the power spectrum of the distortion map, and the motion of optics. In simulations of the dynamic distortion for the PECO telescope, the diffraction spike technique reduces the effects of dynamic distortion by a factor of ~1000 for individual exposures and 10,000 over the mission lifetime due to extensive averaging over tens of hours. [12,13] We apply a reduction factor of 1000 to the 10 mas error in the static distortion map to derive an upper limit of ~10 μas on the systematic error floor. This is a conservative estimate on the systematic error floor because we do not include further averaging beyond a single epoch.

3. RESULTS

3.1 Performance Trends with Number of Reference Stars

We first investigate the relative astrometric precision perpendicular to the zenith vector as a function of the number of reference stars, stellar density, and field size. Figure 2 shows the single-axis, relative astrometric precision on a bright target star ($I = 7$) for a 5-meter telescope and a total integration time of 3 hours. The systematic noise floor due to instrumental jitter is not included to clarify performance below 10 μas.

The astrometric precision is dominated by DTTJ error. A particular feature of this error is that reference stars closer to the target star are more valuable than distant stars because the DTTJ error increases with distance (see Figure 1). Adding

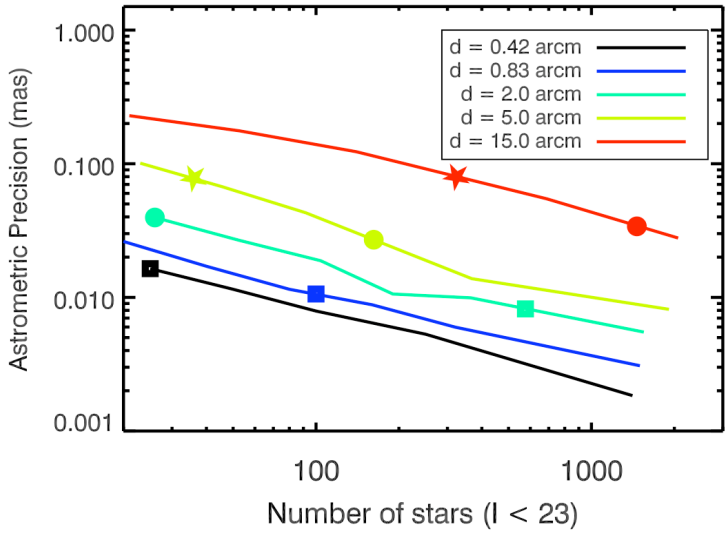

Fig. 2. Relative astrometric error in milliarcseconds as a function of the number of reference stars with $I < 23$ for $D = 5$ meters, a 3 hour total integration time, and a $I = 7$ target star. Colors indicate the diameter of the circular field of view. For a given field size d, the number of stars is changed by increasing or decreasing the background stellar density. Square, circle, and star symbols correspond to fixed stellar densities of 180, 8, and 1.8 stars arcmin^{-2}, similar to those in the Galactic plane (b ~ 1-2°), at intermediate Galactic latitude (b ~ 30°), and at the Galactic poles (b ~ 90°), respectively. The systematic noise floor due to instrumental jitter is not included.

more reference stars to the grid by increasing the stellar density should thus improve performance, as more stars are being added close to the target star. Contrastingly, adding reference stars by increasing the field size and holding stellar density constant should not improve performance significantly, as the stars added are more distant and noisy. These expectations are borne out in Figure 2. For each field diameter, the performance improves with the number of stars as ~ $N^{-0.55}$, as has been noted.[8] At fixed stellar density (shown with square, circle, and starred points), however, the performance is generally flat with field diameter. The exception is at small fields ($d < 2'$), where the performance improves as ~ $d^{-0.5}$ at fixed stellar density. There appears to be little advantage in increasing the field size beyond a diameter of ~5 arcminutes.

Note that DTTJ error averages down to the ~10 μas level in fields with high stellar densities (~180 stars arcmin^{-2}, corresponding to Galactic plane fields).

3.2 Performance Trends with Telescope Diameter and Field Size

We next investigate the relative astrometric performance with a large number of reference stars (stellar density of 40 arcmin^{-2} for $I < 23$, corresponding to a Galactic latitude of 5°), a primary star magnitude of $I = 7$, and a total single-epoch exposure time of 3 hours. The relative astrometric error per coordinate perpendicular to the zenith vector is plotted as a function of telescope diameter for multiple field sizes in Figure 3. DTTJ error dominates for the majority of cases. Residual instrumental jitter due to dynamic distortion error dominates for large fields (d > 8′) on large apertures (D > 6.5 m). The photon error of the reference grid begins to dominate for small fields (d < 1′) on small apertures (D < 1 m).

It is clear from Figure 3 that astrometric error due to DTTJ improves sharply with primary mirror diameter, falling below 10 μas for D ~ 6.5 meters with large fields (d > 4′). A 3 meter telescope reaches ~35 μas with large fields. The astrometric precision obtained with large telescopes over wide fields is not limited by the atmosphere, in agreement with other observational studies.[4] Remarkably, for large fields, the astrometric precision is nearly flat below a telescope diameter of 1 meter. This suggests that small telescopes with large fields of view (d > 4′) can obtain scientifically useful astrometric precision (~ 100-200 μas) on bright stars in modestly dense stellar fields.

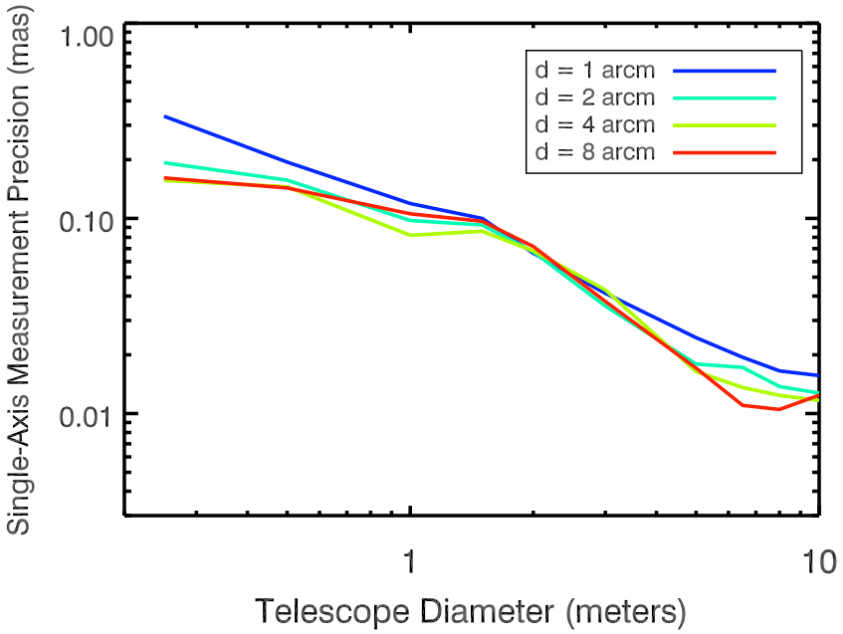

Fig. 3. Total relative astrometric error in milliarcseconds as a function of telescope diameter for a stellar density of 40 stars arcmin^{-2} for $I < 23$ (corresponding to ~5 degrees from the Galactic plane). Only the component of the error perpendicular to the zenith direction is shown. Colors denote different field diameters.

4. SUMMARY

We have used the Cameron, Britton, & Kulkarni (2009)[8] weighting method with the full Differential Tip/Tilt Jitter equation to simulate the astrometric performance of a ground-based, diffractive monopupil telescope and wide-field imager on a bright star. The performance is simulated as a function of target star magnitude I, telescope diameter D, field diameter d, integration time t, zenith angle ξ, and Galactic latitude b. To minimize DAR error, only the component of astrometric error perpendicular to the zenith vector is estimated.

The diffractive pupil and telescope roll techniques[12,13] are included to mitigate instrumental systematic errors due to optical wander, temperature instability, and changing detector quality. With these in place, astrometric performance is seen to penetrate below 100 μas per coordinate, especially for large telescopes (D > 3 meters), fields with high stellar density (> 40 stars arcmin^{-2} with I < 23), and long exposure times (t > 1 hour). In particular, a 3 meter telescope is capable of reaching ~35 μas single-axis relative astrometric error in three hours on a bright target star (I < 10) in fields of moderate stellar density (~40 stars arcmin^{-2} with I < 23). This stellar density corresponds to fields near the Galactic plane, or -5° < b < 5°, giving a sky coverage of ~8%. In addition, small apertures (D < 1 m) can attain 100-200 μas performance with the same stellar density and exposure time. In bright-star astrometry from the ground, there appears to be no advantage to increasing field size beyond ~5′ for a telescope with 0.25 m < D < 10 m unless the photon error on the reference grid is a significant budget term. This can be the case for narrow-band observations or for Galactic pole observations with small telescopes (D < 1 m).
The use of larger fields of view for bright-star astrometry is hampered by dynamic distortion errors and other instrumental jitters, which are expected to increase with field radius. Thus the diffractive pupil technique enables the use of larger fields of view. In addition, because it prevents saturation of the target star, the diffractive pupil enables the use of bright stars (V < 6-10, depending on telescope diameter) as targets.

5. ACKNOWLEDGEMENTS

Thanks to Matthew Britton, Jessica Lu, Michael Shao, Stuart Shaklan, Marie Levine, Jim Burge, Roger Angel, and Tom Milster for contributions and helpful discussions. We recognize support from the NASA APRA program. E.A.B. acknowledges support from the Fulbright Science and Technology program.

REFERENCES

[1] Perryman, M., et al., "GAIA: Composition, formation, and evolution of the Galaxy," A&A, 369, 339 (2001).

[2] Jordi, C., "The European Space Agency GAIA mission: Exploring the Galaxy," proceedings of Astronomy with Megastructures, Joint science with E-ELT and SKA, arXiv:1105.6166 (2011).

[3] Perryman, M., et al., "The Hipparcos Catalogue," A&A, 323, 49 (1997).

[4] Lazorenko, P., "Astrometric Precision of Observations at VLT/FORS2," A&A, 449, 1271 (2006).

[5] Gillessen, S., et al., "Monitoring Stellar Orbits around the Massive Black Hole in the Galactic Center," ApJ, 692, 1075 (2009).

[6] Ghez, A., et al., "Stellar Orbits around the Galactic Center Black Hole," ApJ, 620, 744 (2005).

[7] Pravdo, S. & Shaklan, S., "Astrometric Detection of Extrasolar Planets: Results of a Feasibility Study with the Palomar 5 Meter Telescope," ApJ, 465, 264 (1996).

[8] Cameron, P.B., Britton, M., & Kulkarni, S., "Precision Astrometry with Adaptive Optics," ApJ, 137, 83 (2009).

[9] Lu, J., et al., "Clarifying our View of Star Formation in Massive Young Clusters with Adaptive Optics," UP2010: Have Observations Revealed a Variable Upper End of the Initial Mass Function? ASP Conference Proceedings, 440 (2011).

[10] Fritz, T., et al., "What is limiting near-infrared astrometry in the Galactic Center?" MNRAS, 401, 1177 (2010).

[11] Andersen, J. & King, I., "An Improved Distortion Solution for the Hubble Space Telescope's WFPC2," PASP, 115, 113 (2003).

[12] Guyon, O., et al., "Single aperture imaging astrometry with a diffracting pupil: application to exoplanet mass measurement with a small coronagraphic space telescope," proc. SPIE, 7731, 71 (2010).

[13] Guyon, O., et al., "Diffractive pupil telescope for high-precision space astrometry," proc. SPIE, in press (2011).

[14] Bendek, E., et al., "Dynamic distortion calibration using a diffracting pupil: high precision astrometry laboratory demonstration for exoplanet detection," proc. SPIE, in press (2011).

[15] Bahcall, J., & Soneira, R., "The universe at faint magnitudes. I - Models for the galaxy and the predicted star counts," ApJS, 44, 73 (1980).

[16] Lucas, P., et al., "The UKIDSS Galactic Plane Survey," MNRAS, 391, 136 (2008).

[17] Schlegel, D., et al., "Maps of Dust Infrared Emission for Use in Estimation of Reddening and Cosmic Microwave Background Radiation Foregrounds," ApJ, 500, 525 (1998).

[18] Sasiela, R.J. [Electromagnetic Wave Propagation in Turbulence: Evaluation and Application of Mellin Transforms], 2nd edition, SPIE press, Bellingham, Washington, pp. 170-171 (2007).

[19] Neyman, C., "Atmospheric Parameters for Mauna Kea," Keck Adaptive Optics Note #303 (2004).

[20] Lindegren, L., in IAU Colloq. 48, Modern Astrometry, ed. F.V. Prochazka & R.H. Tucker, Kluwer, Dordrecht, 197 (1978).

[21] Gubler, J. & Tytler, D., "Differential Atmospheric Refraction and Limitations on the Relative Astrometric Accuracy of Large Telescopes," PASP, 110, 738 (1998).

[22] Lu, J., et al., "Recent results and perspectives for precision astrometry and photometry with adaptive optics," proc. SPIE, 7736, 51 (2010).

[23] Yelda, S., et al., "Improving Galactic Center Astrometry by Reducing the Effects of Geometric Distortion," ApJ, 725, 331 (2010).

[24] Chambers, K. C., "Astrometry with Pan-STARRS and PS1: Pushing the limits of atmospheric refraction, dispersion, and extinction corrections for wide-field imaging," in ASP Conf. Ser. 338: Astrometry in the Age of the Next Generation of Large Telescopes, ed. P. K. Seidelmann & A. K. B. Monet (2005).

[25] Anderson, J. & King, I.R, "Toward High-Precision Astrometry with WFPC2. I. Deriving an Accurate Point-Spread Function," PASP, 112, 1360 (2000).

[26] Trippe, S., et al., "High-Precision Astrometry with MICADO at the European Extremely Large Telescope," MNRAS, 402, 1126 (2010).

[27] Diolaiti, E., et al., "Analysis of isoplanatic high resolution stellar fields by the StarFinder code," A&AS, 147, 335 (2000).

This work performed under the auspices of the U.S. Department of Energy by Lawrence Livermore National Laboratory under Contract DE-AC52-07NA27344.